ACS APPLIED MATERIALS & INTERFACES

RESEARCH ARTICLE

www.acsami.org

Schottky Barrier Mediated Single-Polarity Resistive Switching in Pt Layer-Included TiO_x Memory Device

Yu-Lung Chung, Pei Ying Lai, Ying-Chiuan Chen, and Jen-Sue Chen*

Department of Materials Science and Engineering, National Cheng Kung University, No.1, University Road, Tainan City 701, Taiwan

Supporting Information

ABSTRACT: A distinct unipolar but single-polarity resistive switching behavior is observed in a TiO_x/Pt/TiO_x trilayer structure, formed by thermal oxidation of a Ti/Pt/Ti stack. As a comparison, a memory device with a single TiO_x active layer (without addition of Pt midlayer) is also fabricated but it cannot perform resistive switching. Energy band diagrams are illustrated to realize the modulation of Schottky barrier junctions and current conduction in TiO_x-based devices under various biasing polarities. Introduction of the Pt midlayer creates two additional Schottky barriers, which mediate the band bending potential at each metal-oxide interface and attains a rectifying current conduction at the high-resistance state. The rectifying conduction behavior is also observed with an AFM-tip as the top electrode, which implies the rectifying property is still valid when miniaturizing the device to nanometer scale. The current rectification consequently leads to a single-polarity, unipolar resistive switching and electrically rewritable performance for the TiO_x/Pt/TiO_x device.

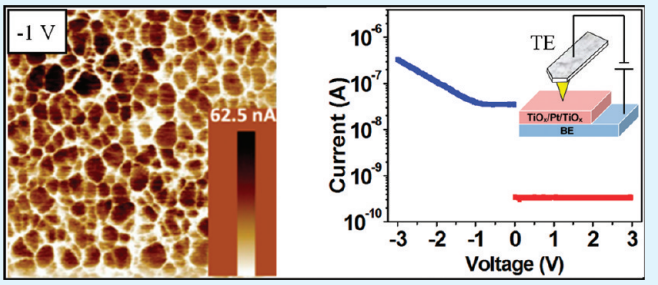

KEYWORDS: resistive switching, TiO_x, rectify, conductive atomic force microscopy, Schottky barrier, RRAM

INTRODUCTION

Among the emerging candidates for nonvolatile memories, resistive switching in metal−insulator−metal (MIM) structures receives great attention because their electrical states can be altered reversibly and reproducibly simply by the application of a voltage. The electrical bistability switching behavior in MIM structures is observed for a wide variety of insulating materials and applied as resistance random access memories (RRAMs). Many of binary transition metal oxides, such as NiO,[1−4] TiO_2,[5−7] ZnO,[8] and ZrO_2[9] have been investigated as the active layers application in RRAMs. Regarding to the resistive switching mechanism, several models have been proposed. For example, the change of resistance states depending on arrangement of the defects (oxygen vacancies),[10,11] local redox process based on oxygen vacancy migration (or oxygen ion diffusion) induced by opposite bias,[12,13] formation and rupture of localized metallic bridge by the anode dissolution and cathodic deposition of the electrode materials under an electric field,[14,15] or the resistance change because of field-induced change of Schottky junction at the oxide/electrode interface.[16,17]

Presence of Schottky junctions implies the possibility of fabricating MIM devices possessing not only resistive switching, but also current rectifying characteristics, without employing the one diode and one resistor (1D-1R),[18,19] or one transistor and one resistor (1T-1R) architecture.[20] Dual-function (resistive switching plus rectifying) RRAM devices have been recently reported using TiO_x-based MIM structure.[21,22] Both works attribute the rectifying characteristics to Schottky junctions at the electrode/oxide interfaces and the Schottky junction is regarded straightforwardly as a diode. However, in addition to the forward or reverse bias effect, the depletion region of a metal-oxide Schottky junction may be enhanced or eliminated by the field-driven movement of oxygen vacancies, because oxygen vacancies are positively charged and associated with the production of electron carriers (i.e., as donor dopants in n-type oxides).[23] A significant example is the field-programmable rectification in TiO_2 crystal based on the field-induced modification of Schottky junctions.[24] Therefore, it is intriguing to explore the correlation between the Schottky junction modulation and the rectifying resistive switching performance, both related with the field-induced migration of oxygen vacancies, in MIM devices.

In this work, we report an investigation on a Pt layer-included TiO_x (of the TiO_x/Pt/TiO_x stacking structure, formed by thermal oxidation of Ti/Pt/Ti films) memory device which exhibits an unipolar but single-polarity resistive switching behavior and showed electrically rewritable property. As a comparison, a memory device with a single TiO_x active layer (formed by thermal oxidation of a Ti film without addition of Pt midlayer) is also fabricated and characterized. Energy band diagrams are illustrated to realize the modulation of Schottky junctions and current conduction in TiO_x-based devices under various biasing polarities. In addition to the variation of Schottky barrier depletion width by the accumulation or diminution of oxygen vacancies at the electrode/TiO_x interfaces, the Pt midlayer creates two extra Schottky junctions to mediate the potential drop across the TiO_x/Pt/TiO_x stacking

Received: January 28, 2011
Accepted: May 17, 2011
Published: May 17, 2011

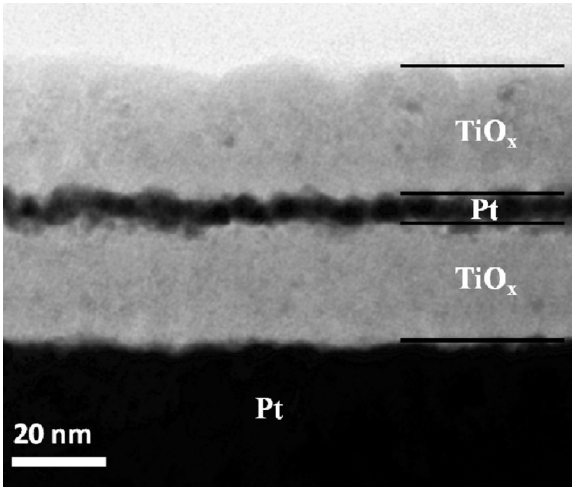

Figure 1. Cross-sectional TEM micrograph of the TiO_x/Pt/TiO_x film formed by annealing the Ti/Pt/Ti stack at 500 °C in oxygen ambient.

structure. As a result, rectifying current conduction is attained in the TiO_x/Pt/TiO_x device and the rectification behavior leads to a single-polarity, unipolar resistive switching performance. The rectification behavior is also observed with an AFM-tip as the top electrode. This unique electrical performance implies the possibility of miniaturizing the devices to nanometer scale.

RESULTS AND DISCUSSION

Figure 1 displays cross-sectional transmission electron microscopy (TEM) micrograph of the TiO_x/Pt/TiO_x layers. The dark-contrasted Pt layer is embedded in the TiO_x matrix and its thickness is about 9 nm. The TiO_x/Pt/TiO_x active layer is form by oxidizing the Ti/Pt/Ti stack at 500 °C. As compared to the as-deposited Ti/Pt/Ti stack (see Figure S1 in the Supporting Information), the volume dilatability of the Ti layer to TiO_x layer during oxidation is about 1.45, while the Pt midlayer is not affected basically. On the basis of the crystallographic data of hexagonal close-packed Ti and rutile TiO_2, the ideal volume expansion from Ti to TiO_2 is equal to 1.77. The volume dilatability indicates that the TiO_x film is not a stoichiometric TiO_2.

Regarding to the film crystallinity, grazing incident angle X-ray diffraction (GIAXRD) analysis suggests that both TiO_x and TiO_x/Pt/TiO_x films in this study reveal a polycrystalline rutile structure (see Figure S2 in the Supporting Information). However, the low diffraction intensity also suggests the crystal size shall be small and part of TiO_x in the films may be amorphous.

Figure 2 shows the $I-V$ characteristics of the TiO_x and TiO_x/Pt/TiO_x memory devices (with Pt as both top and bottom electrodes) under a direct current (dc) bias sweeping mode, in which the bias voltage was applied on the top electrode (abbreviated as "TE" hereafter) while the bottom electrode (abbreviated as "BE" hereafter) was grounded. In Figure 2a, it is apparent that the TiO_x-only device keeps at the high-resistance state (HRS, i.e. off state) and the current is below 1×10^{-6} A with either positive (0 to 8 V) or negative (0 to −8 V) voltage sweeping. In contrast, Figure 2b reveals that the $I-V$ curve of the TiO_x/Pt/TiO_x memory device under a negative bias sweeping (Figure 2b, curve (1)) displays a low current level of below 1×10^{-5} A from 0 to −8 V and it cannot be switched to LRS. When sweeping at positive bias, the current increases more steeply and the TiO_x/Pt/TiO_x device can be switched to a low-resistance state (LRS,

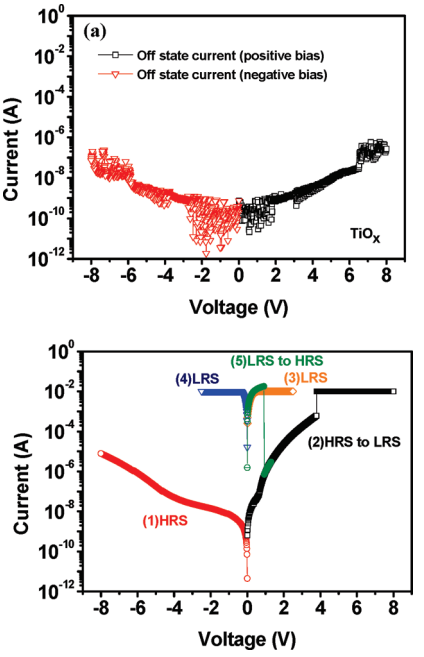

Figure 2. (a) $I-V$ characteristics of the TiO_x memory devices in semilog scale when the voltage is sweeping in positive bias and negative bias, and (b) $I-V$ characteristics of the TiO_x/Pt/TiO_x memory device when the voltage is sweeping in both positive and negative bias polarities. The number labeled on each curve indicates the sweeping sequence.

i.e. on state) when the set voltage (~3.7 V) is reached (curve (2)). The LRS current is limited by a compliance value (I_{comp} = 0.01A) to prevent permanent dielectric breakdown. Once the transition is achieved, the device remains at the LRS even after the applied voltage is removed, as revealed by the subsequent bias sweeping under positive bias and negative bias sweeping (curve (3) and curve (4) of Figure 2b), which indicates the nonvolatile switching property. When the current compliance is released to 0.1 A (I_{comp} = 0.1 A), the device can be switched back to the HRS by the application of a positive voltage ~0.9 V, which is below the set voltage (curve 5). A reproducible resistive switching behavior is achieved in the memory device. Besides, no initial electrical forming process is needed for our fresh devices to complete the resistive switching (see the Figure S3 in the Supporting Information). The TiO_x/Pt/TiO_x device possesses the electrical bistability when applying the positive bias and it exhibits a rectifying behavior; however, the rectifying behavior exists only in HRS. Once the device is switched to LRS, the conducting filaments form within the active layer and Ohmic conduction behavior is observed in LRS as the current transport via these conducting paths (Figure 2b, curves 3 and 4). Therefore, the rectifying behavior exists only in HRS, but not in LRS. As a result, our TiO_x/Pt/TiO_x memory device exhibit a "single-polarity switching" behavior, which is unique and will be further investigated in the following discussions. To appraise the potential of this device for nonvolatile memory application, we have examined the stability of cells with the TiO_x/Pt/TiO_x active layer at LRS and HRS by retention test. Both LRS and HRS are well-maintained for more than 1×10^4 seconds in the retention test (see Figure S4 in the Supporting Information).

To further explore the "single-polarity switching" behavior, we have conducted conductive atomic force microscopy (C-AFM) measurement to probe the current−voltage relationship in

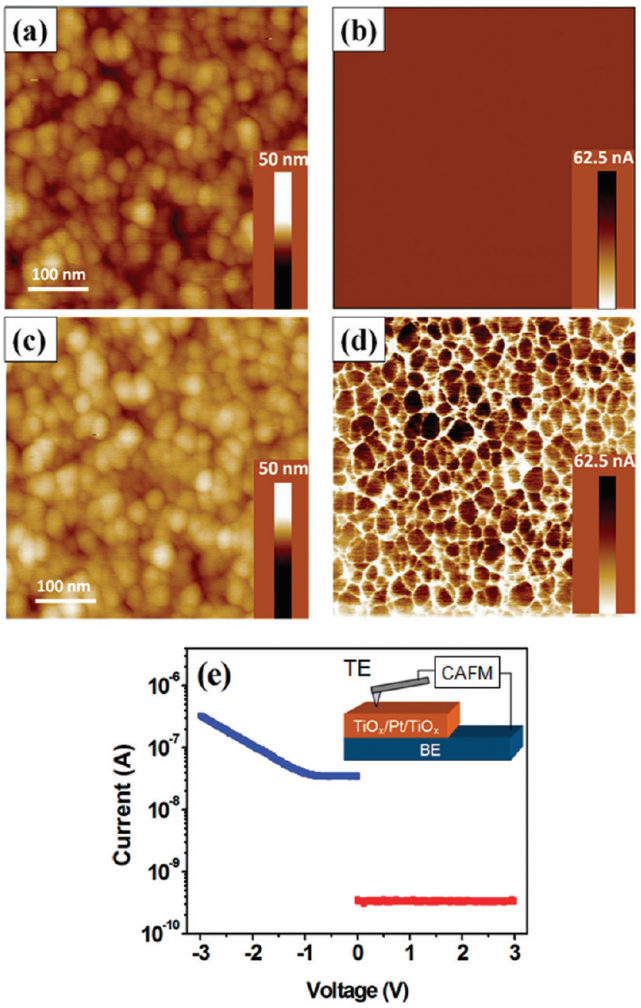

Figure 3. C-AFM images obtained by scanning the Cr/Pt-coated tip on the TiO_x/Pt/TiO_x/Pt(BE) sample. (a) Topography image and (b) current mapping image when biasing +1 V on the Pt BE. (c) Topography image and (d) current mapping image when biasing −1 V on the Pt BE. The maximum current is 62.5 nA for C-AFM measurement. (e) $I-V$ characteristic a single-point C-AFM measurement by sweeping bias in the range of ±3 V. The inset figure shows a schematic illustration of setup for the measurement.

micro-to-nano scale area. In C-AFM measurement, the voltage bias is applied on the Pt BE and current is read through a scanning tip (serving as the TE) in contact with the active layer. Before performing C-AFM measurement on devices, the conductivity of C-AFM tip is confirmed by placing it on highly ordered pyrolytic graphite (HOPG). The current measurement is done at the same time as the topography scan is obtained. Figure 3 displays the topography images (scanning area 0.5 × 0.5 μm^2) and current mapping images of the TiO_x/Pt/TiO_x/Pt(BE) sample. When applying a bias of +1 V or −1 V on the BE, we obtained similar topography images, as presented in images a and c in Figure 3, and the root-mean-square roughness (R_{rms}) values are both 1.7 nm. When a bias of +1 V is applied on the BE of device, the whole scanned area exhibits uniformly low current (Figure 3b). On the contrary, a substantial current is detected when a bias of −1 V is applied to the BE of device, as shown in Figure 3d. The current image also reflects the surface topography because the surface roughness influences the pressure exerted on the tip and results in variation of the detected current. After obtaining the topography and current mapping images, we conducted a single-point C-AFM I−V measurement by sweeping the BE bias from 0 to +3 V and from 0 to −3 V, as presented in Figure 3e. The current is constant and rather low (~3×10^{-10} A) from 0 to 3 V, whereas the current increase as the negative bias increasing from 0 to −3 V ($I = 3 \times 10^{-7}$ A at −3 V). This result confirms the rectifying I−V character of TiO_x/Pt/TiO_x device shown in Figure 2b. The discontinuous current around 0 V is observed in our CAFM measurement (Figure 3e). Basically, the current with an infinitesimal increase of voltage should be continuous and have a similar value whether under a positive bias or a negative bias. This phenomenon of discontinuous current around 0 V is also observed in the literatures.[25−27] Crupi et al.[27] reported that the interface defect states may be a possible reason which affects electron tunneling and leads discontinuous current at 0 V. Even though it is somewhat arbitrary because it cannot be verified in a straightforward way. In addition, the area of TE pad of the devices for Agilent 4156C analyzer measurement is 4×10^4 μm^2, which is much larger than the tip area in C-AFM measurement (about 4×10^{-3} μm^2). The estimated current densities from pad-electrode measurement and CAFM are 0.25 A/cm^2 (with +3 V on TE) and 7500 A/cm^2 (with −3 V on BE), respectively. The difference may from the sharpness of the AFM tip which enhances the local electric field. Choi et al.[28] reported the HRS current densities measured by pad-electrode I−V measurement and CAFM were 0.038 A/cm^2 and 200 A/cm^2, respectively. The difference in the current density is about 4 orders of magnitude, which is similar to our result. The CAFM result suggests that the rectification shall be associated with a homogeneous physics picture all over the device area, and shall not depend on the local defects at TiO_x/Pt interfaces or within the TiO_x layer. Also, the observation gives a point of view that the rectifying $I-V$ behavior of TiO_x/Pt/TiO_x device is still valid when the device size is miniaturized to nanometer scale. However, we cannot locally switch on the TiO_x/Pt/TiO_x device with AFM-tip due to the instrument limitation. The maximum current of our CAFM is 1×10^{-6} A, which corresponds to a current density of about 5×10^4 A/cm^2 but is still not high enough for filamentary switching (~1×10^7 A/cm^2 [10]).

Chemical bonding state of TiO_x is investigated by using X-ray photoelectron spectrometer (XPS). Figure 4 shows the Ti 2p XPS spectra (Ti $2p_{1/2}$ and Ti $2p_{3/2}$ doublet peaks) at TE/TiO_x and BE/TiO_x interfaces of the TiO_x and TiO_x/Pt/TiO_x samples. The spectra have been calibrated for the charging effect with reference to Pt $4f_{7/2}$ peak at 71.2 eV.[29] The spectra are deconvoluted to three pairs of Ti 2p doublet peaks pertaining to three oxidation states: Ti^{4+} (TiO_2), Ti^{3+} (Ti_2O_3), Ti^{2+} (TiO). The Ti $2p_{3/2}$ peaks associated with Ti^{4+}, Ti^{3+}, and Ti^{2+} are located at 459.0 ± 0.1,[29] 457.4 ± 0.1,[30] and 455.6 ± 0.1 eV,[31] respectively. The XPS analysis indicates that there exist oxygen vacancies in the TiO_x layer of both TiO_x-only and TiO_x/Pt/TiO_x samples.

Oxygen vacancies are the common intrinsic defects in titanium oxide and considered donors in n-type semiconductor.[23] However, the vacancy energy levels are rather far away from the edge of TiO_2 conduction band,[32] the ionization probability is low. The electron concentration will relate with the oxygen vacancy concentration but not in a 1:1 fashion. Based on the Ti 2p XPS spectra (Figure 4), the oxygen vacancy concentrations at different interfaces of the TiO_x and TiO_x/Pt/TiO_x devices can be represented by the sum of intensity for Ti^{3+} and Ti^{2+} signals, as shown in Table 1. According to Table 1, oxygen vacancy

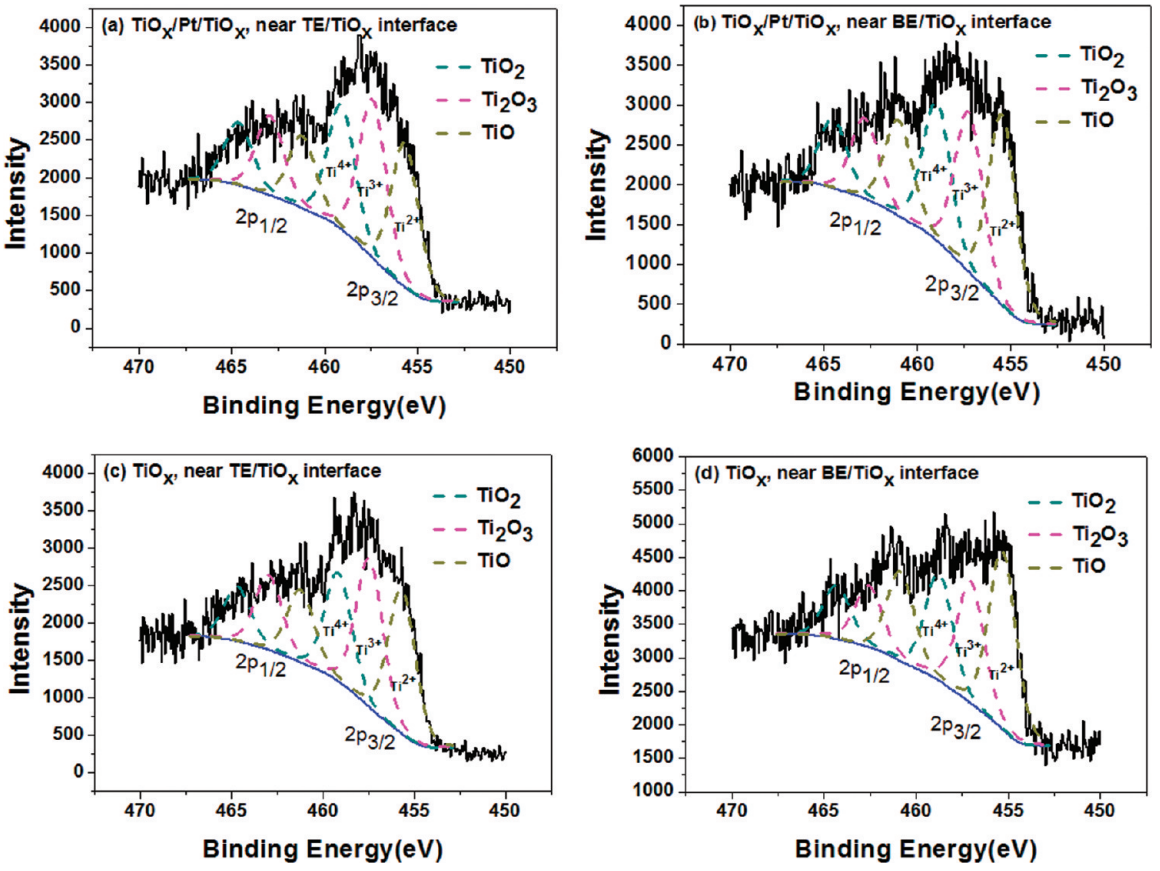

Figure 4. Ti 2p XPS spectra taken from (a) TE/TiO_x interface of TiO_x/Pt/TiO_x sample, (b) BE/TiO_x interface of TiO_x/Pt/TiO_x sample, (c) TE/TiO_x interface of TiO_x sample, (d) BE/TiO_x interface of TiO_x sample.

Table 1. Calculated Peak Area of Ti^{3+} and Ti^{2+} XPS Signals for Each Interface in TiO_x and TiO_x/Pt/TiO_x Samples

	XPS peak area		
sample	Ti^{3+}	Ti^{2+}	total area Ti^{3+}+ Ti^{2+}
TiO_x (TE)	6273.1	5677.0	11950.1
TiO_x (BE)	5982.5	7091.9	13074.4
TiO_x/Pt/TiO_x (TE)	5927.6	5744.8	11672.4
TiO_x/Pt/TiO_x (BE)	5630.2	7884.0	13514.2

concentration is higher at BE/TiO_x interface than at TE/TiO_x interface for both samples. In addition, oxygen vacancy concentrations at TE/TiO_x interfaces in both samples are almost identical and so are the oxygen vacancy concentrations at BE/TiO_x interfaces.

Because XPS analysis indicates the variation of oxygen vacancies at different interfaces, the oxygen vacancy concentration in both TiO_x and TiO_x/Pt/TiO_x should exhibits a gradient distribution (lower vacancy concentration nearby TE, higher vacancy concentration nearby BE), as schematically shown in Figure 5a. In addition, the Pt/TiO_x interface shall form a Schottky contact because the work function of Pt is 5.65 eV,[33] and Fermi level of n-type TiO_x is about 4.7−5.2 eV, which is close to the conduction band edge of TiO_2.[34] The energy band diagram of the TiO_x/Pt/TiO_x stack at the initial thermal equilibrium state is accordingly drawn as Figure 5b. As demonstrated by Yang et al.,[5] positively charged oxygen vacancies are driven toward the TE by the electric field when a negative bias is applied on TE, as schematically shown in Figure 5c. Migration of oxygen vacancies increases the electron concentration (proportional to charge density) at the TE/TiO_x interface and reduces the depletion width. However, the variation of Schottky junction depletion width (i.e., the curvature of band bending) depends on both charge density and applied bias across the junction. Additionally, when a bias is applied across a metal(BE)/semiconductor/metal(TE) device, the potential drop across device is mainly shared by the Fermi level offset between metal and semiconductor at both TE and BE interfaces, which leads to the change of band bending potential in semiconductor near the TE and BE interfaces. In a Pt/TiO_x/Pt device, since Pt forms Schottky junction with TiO_x, the applied bias will contribute to a forward bias and a reverse bias on the two Pt/TiO_x junctions (i.e., $V_{applied} = V_{forward} + V_{reverse}$). Therefore, by applying a negative (reverse) bias on TE, the band bending potential in TiO_x layer is increased ($V_{band\ bending} = V_{built\text{-}in} + V_{reverse}$) and the depletion region is widened. Thus, the opposite effects (increase of charge density by collection of oxygen vacancies vs reverse bias) will cancel each other and the depletion width at the TE/TiO_x interface remains substantially wide, as revealed by the schematic energy band diagram in Figure 5d. The wide depletion region makes electrons difficult to tunnel from TE into TiO_x, leading to the suppression of current when a negative bias is applied on TE. This scenario is suitably applied to both TiO_x and TiO_x/Pt/TiO_x devices. It should be noted that although the potential drop across device is primarily shared by

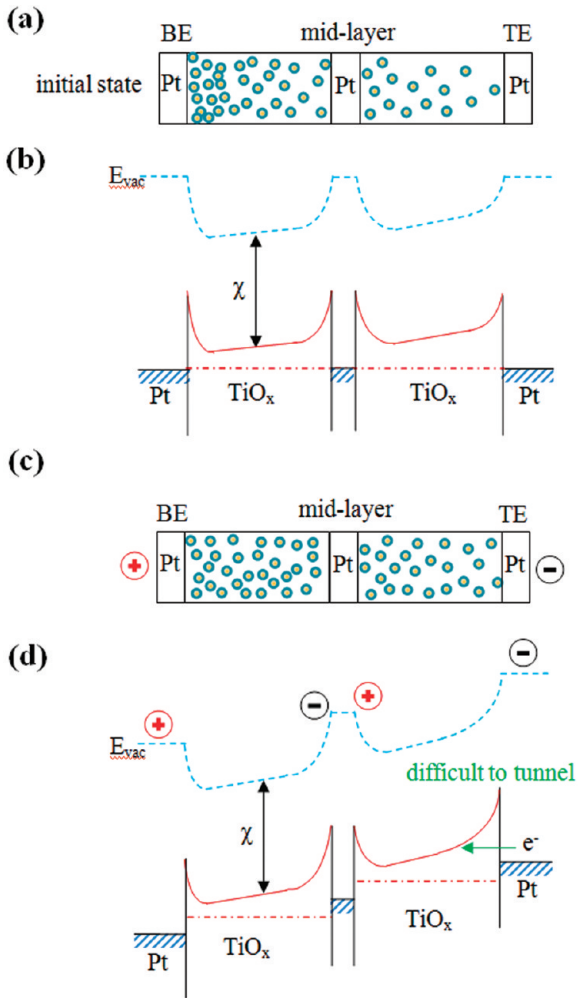

Figure 5. (a) Schematic illustration of oxygen vacancy (represented by the circular dots) distribution in TiO_x/Pt/TiO_x device at initial thermal equilibrium state. (b) Energy band diagram of the TiO_x/Pt/TiO_x device at initial thermal equilibrium state. (c) Schematic illustration for the distribution of oxygen vacancies when applying a negative bias on TE. (d) Energy band diagram when applying a negative bias on TE.

the change of band bending potential at each Pt/TiO_x interface, the electric field is still existing within the bulk semiconductor (away the depletion region). Thus, the driving force for the oxygen migration is the electric field outside the depletion region.

When applying a positive bias on TE, it is equivalent to apply a negative bias on BE. Similar to the previous case, oxygen vacancies move to the BE/TiO_x interface by the electric field, as depicted by the schematic in Figure 6a. Analogously, the depletion region at BE/TiO_x interface is narrowed and in the mean time, the negative (reverse) bias on BE will increase the band bending potential in TiO_x layer and ($V_{band\ bending} = V_{built\text{-}in} + V_{reverse}$) consequently widen the depletion of the BE/TiO_x junction region. The two effects may again cancel each other. However, the depletion width of the BE/TiO_x junction will be rather narrow due the initially high oxygen vacancy concentration at the BE/TiO_x interface. Therefore, it is possible for electrons to tunnel through the BE/TiO_x Schottky barrier, as revealed by the schematic energy band diagram in Figure 6b. Therefore, a higher HRS current is observed when applying a positive bias on the TE of the TiO_x/Pt/TiO_x device (Figure 2b, positive bias side).

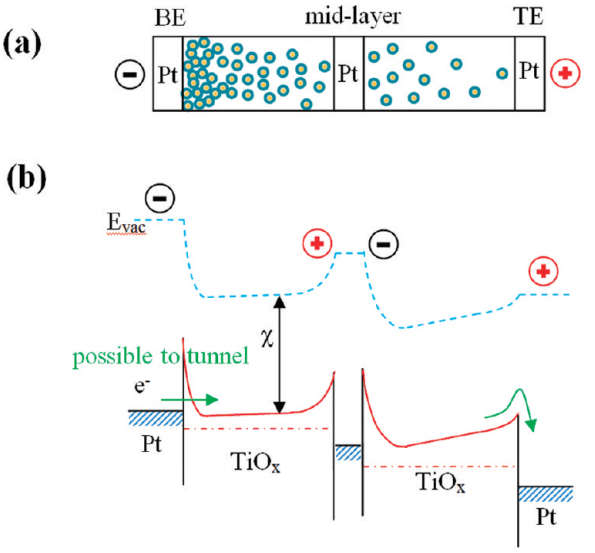

Figure 6. (a) Schematic illustration for the distribution of oxygen vacancies in the TiO_x/Pt/TiO_x device when applying a positive bias on TE. (b) Energy band diagram of the TiO_x/Pt/TiO_x device when applying a positive bias on TE.

As for the TiO_x device, the current remains rather low when applying a positive bias on TE (Figure 2a). The depletion width at the BE/TiO_x interface in both TiO_x and TiO_x/Pt/TiO_x devices is widened due to the increase of band bending potential by applying a negative bias on BE (equivalent to a positive bias on TE). However, the depletion width at the BE/TiO_x interface in TiO_x/Pt/TiO_x device should be narrower than that in TiO_x device. The difference between our TiO_x and TiO_x/Pt/TiO_x devices is the intermediate Pt layer. Because the potential across a metal/semiconductor/metal device is mainly shared by the change of band bending potential of metal/semiconductor junctions, the intermediate Pt layer in TiO_x/Pt/TiO_x device creates two additional Schottky barriers and they will assist to share the overall potential drop between the TE and BE, meaning that the forward or reverse bias exerted at each Pt/TiO_x interface in TiO_x/Pt/TiO_x device is less than that in TiO_x device. Therefore, although the oxygen vacancy concentrations are comparable for the two devices, the band bending at the BE/TiO_x Schottky junction of TiO_x/Pt/TiO_x device remains steep-and-narrow while that of the TiO_x device is broadened by a larger reverse bias. As a result, the depletion region in the BE interface of the TiO_x/Pt/TiO_x device stays narrow, as illustrated by the schematic energy band diagrams in Figure 7, and the device exhibits a higher electron current than the pure TiO_x device does. In contrast, the electrons are not able to tunnel from BE into TiO_x active layer in the TiO_x device and the device exhibits symmetrically low current for both positive and negative voltage scannings. One may consider whether the smaller band bending potential at the BE/TiO_x interface of the TiO_x/Pt/TiO_x device would affect the probability for electron tunneling through the interface. According to the equation of tunneling probability of electrons through an energy barrier,[35] it is the barrier width which plays an important role for electron tunneling probability. Therefore, we take the depletion width to be the major factor for electron tunneling through the Schottky barrier.

Regarding to the resistive switching mechanism of TiO_x/Pt/TiO_x device, we suggest that the resistive switching behavior is

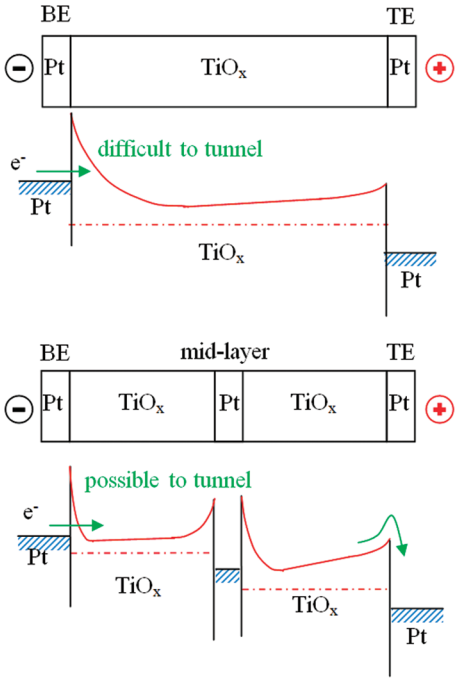

Figure 7. Energy band diagrams illustrating the differences in depletion width for TiO_x and $TiO_x/Pt/TiO_x$ devices when applying a positive bias on TE.

originated from the formation and rupture of conducting filaments composed of oxygen vacancies. Kim et al.[36,37] reported a filamentary switching mechanism of a $Pt/TiO_2/Pt$ capacitor which exhibited a unipolar switching behavior. Their experimental result suggests that the conducting paths propagate from the cathode (negatively biased electrode) to the anode (positively biased electrode) and form "tree-shaped (or conical shape)" filaments, which are thicker and stronger near the cathode interface than near the anode interface. Therefore, rupture and recovery of filaments are in the localized region near the anode.

For our $TiO_x/Pt/TiO_x$ device, when a positive bias is applied on TE, positively charged oxygen vacancies migrate toward to BE and accumulate from BE to TE to form the conducting filament. Analogous to Kim's work, the filaments are possibly in tapering shape (thick/strong near by cathode (the BE) and thin/weak near by anode (TE)). The construction of filament is only possible for the $Pt/TiO_x/Pt$ device at positive bias sweeping because its intrinsically higher HRS current will produce the thermal energy to assist alignment of oxygen vacancies.

During the reset process, the conduction filaments are disrupted via the Joule heating near TE (i.e., the anode, where the filament is thin and weak) after releasing the current compliance. The reset process is unlikely to happen by reversing the bias polarity (i.e., applying a negative bias on TE) because the oxygen vacancy concentration near BE is high when the filament has been built. It is not easy to deplete oxygen vacancies away from BE; therefore, the switching behavior is unipolar but not bipolar.

CONCLUSION

In conclusion, a single-polarity, unipolar resistive switching character, originated from the asymmetrical (i.e., rectifying) HRS current at different voltage polarities, is demonstrated with the Pt metal embedded TiO_x (i.e., $TiO_x/Pt/TiO_x$) device. The conductance ratio between the HRS and LRS is about 10^5. Introduction of Pt midlayer creates two additional Schottky barriers, which mediates the band bending potential in oxide at each Pt/TiO_x interface and ensures the current rectification in the $TiO_x/Pt/TiO_x$ device. The single-polarity switching behavior is a combination of bias-induced Schottky barrier modification and conduction filament construction, both associated with the bias-driven migration of oxygen vacancies. The rectifying performance is also valid with a nanoscale sized electrode (the AFM tip), which opens a possibility for the implement of the $TiO_x/Pt/TiO_x$ memory cells to high-density, single-polarity, unipolar switching RRAM arrays. Our memory device demonstrates the rectifying switching behavior without serial connection of any additional device, which simplifies the fabrication process and is also possible to achieve the nanoscale memory cell arrays.

EXPERIMENTAL METHODS

Ti/Pt/Ti stacking layers with thickness of 20/9/20 nm were deposited on $Pt(BE)/Ti/SiO_2/Si$ substrates by sputtering. The Ti/Pt/Ti stacks were subsequently oxidized at 500 °C for 30 min in oxygen ambient to form Pt-included TiO_x films as RRAM active layers. To verify the role of Pt layer in resistive switching behavior, TiO_x active layers without the Pt midlayer were fabricated by oxidizing a single Ti layer (~45 nm) in the same process. The crystalline phases in the active layer were identified by GIAXRD (Rigaku D/MAX2500) using Cu Kα radiation (λ=0.1542 nm) and an incident angle of 3°. The cross-sectional microstructure of the $TiO_x/Pt/TiO_x$ films was investigated by TEM (JEOL 2100F). Chemical bonding states in the $TiO_x/Pt/TiO_x$ films were characterized with XPS (VG ESCA Scientific Theta Probe). For electrical properties measurement, the memory devices employed Pt as top electrode with area of 0.04 mm^2 and thickness of 150 nm deposited by sputtering through a shadow mask. Agilent 4156C precision semiconductor parameter analyzer was employed to measure the resistive switching behavior of TiO_x and $TiO_x/Pt/TiO_x$ memory devices at room temperature. C-AFM (Vecco Innova) measurements were performed at room temperature and atmospheric pressure. A conductive tip (Cr/Pt-coated Si tip ContE (model) from budget sensors, with a curvature radius <25 nm) was used for local area C-AFM measurement operating in contact mode. The tip was grounded and scanning across the active layer surface and a bias was applied on the bottom electrode.

ASSOCIATED CONTENT

Supporting Information. Figures of material analysis including TEM image and GIAXRD patterns; additional $I-V$ characteristics and stress test of $TiO_x/Pt/TiO_x$ memory device. This material is available free of charge via the Internet at http://pubs.acs.org/.

AUTHOR INFORMATION

Corresponding Author

*Telephone: +886-6-2757575, ext. 62948. Fax: +886-6-2762541. E-mail: jenschen@mail.ncku.edu.tw.

ACKNOWLEDGMENT

The authors gratefully appreciate the financial support from the National Science Council of Taiwan (Grant NSC-96-2628-E-006-013-MY3), NCKU Landmark Project (A0051), and Applied Materials Taiwan.

REFERENCES

(1) Goux, L.; Lisoni, J. G.; Jurczak, M.; Wouters, D. J.; Courtade, L.; Muller, C. *J. Appl. Phys.* **2010**, *107*, 024512.

(2) Seo, S.; Lee, M. J.; Seo, D. H.; Jeoung, E. J.; Suh, D. S.; Joung, Y. S.; Yoo, I. K.; Hwang, I. R.; Kim, S. H.; Byun, I. S.; Kim, J. S.; Choi, J. S.; Park, B. H. *Appl. Phys. Lett.* **2004**, *85*, 5655–5657.

(3) Seo, S.; Lee, M. J.; Seo, D. H.; Choi, S. K.; Suh, D. S.; Joung, Y. S.; Yoo, I. K.; Byun, I. S.; Hwang, I. R.; Kim, S. H.; Park, B. H. *Appl. Phys. Lett.* **2005**, *86*, 093509.

(4) Seo, S.; Lee, M. J.; Kim, D. C.; Ahn, S. E.; Park, B. H.; Kim, Y. S.; Yoo, I. K.; Byun, I. S.; Hwang, I. R.; Kim, S. H.; Kim, J. S.; Choi, J. S.; Lee, J. H.; Jeon, S. H.; Hong, S. H. *Appl. Phys. Lett.* **2005**, *87*, 263507.

(5) Park, W. Y.; Kim, G. H.; Seok, J. Y.; Kim, K. M.; Song, S. J.; Lee, M. H.; Hwang, C. S. *Nanotechnology* **2010**, *21*, 195201.

(6) Yang, J. J.; Pickett, M. D.; Li, X. M.; Ohlberg, D. A. A.; Stewart, D. R.; Williams, R. S. *Nat. Nanotechnol.* **2008**, *3*, 429–433.

(7) Kim, K. M.; Kim, G. H.; Song, S. J.; Seok, J. Y.; Lee, M. H.; Yoon, J. H.; Hwang, C. S. *Nanotechnology* **2010**, *21*, 305203.

(8) Lee, S.; Kim, H.; Yun, D. J.; Rhee, S. W.; Yong, K. *Appl. Phys. Lett.* **2009**, *95*, 262113.

(9) Lin, C. Y.; Wu, C. Y.; Tseng, T. Y.; Hu, C. M. *J. Appl. Phys.* **2007**, *102*, 094101.

(10) Kwon, D. H.; Kim, K. M.; Jang, J. H.; Jeon, J. M.; Lee, M. H.; Kim, G. H.; Li, X. S.; Park, G. S.; Lee, B.; Han, S.; Kim, M.; Hwang, C. S. *Nat. Nanotechnol.* **2010**, *5*, 148–153.

(11) Jeong, H. Y.; Lee, J. Y.; Choi, S. Y. *Appl. Phys. Lett.* **2010**, *97*, 042109.

(12) Kinoshtia, K.; Okutani, T.; Tanaka, H.; Hinoki, T.; Yazawa, K.; Ohmi, K.; Kishida, S. *Appl. Phys. Lett.* **2010**, *96*, 143505.

(13) Waser, R.; Dittmann, R.; Staikov, G.; Szot, K. *Adv. Mater.* **2009**, *21*, 2632–2663.

(14) Xu, Z.; Bando, Y.; Wang, W. L.; Bai, X. D.; Golberg, D. *ACS Nano* **2010**, *4*, 2515–2522.

(15) Hsiung, C. P.; Liao, H. W.; Gan, J. Y.; Wu, T. B.; Hwang, J. C.; Chen, F.; Tsai, M. J. *ACS Nano* **2010**, *4*, 5414–5420.

(16) Sawa, A.; Fujii, T.; Kawasaki, M.; Tokura, Y. *Appl. Phys. Lett.* **2004**, *85*, 4073–4075.

(17) Asanuma, S.; Akoh, H.; Yamada, H.; Sawa, A. *Phys. Rev. B* **2009**, *80*, 235113.

(18) Lee, M. J.; Park, Y.; Suh, D. S.; Lee, E. H.; Seo, S.; Kim, D. C.; Jung, R.; Kang, B. S.; Ahn, S. E.; Lee, C. B.; Seo, D. H.; Cha, Y. K.; Yoo, I. K.; Kim, J. S.; Park, B. H. *Adv. Mater.* **2007**, *19*, 3919–3923.

(19) Cho, B.; Kim, T. W.; Song, S.; Ji, Y.; Jo, M.; Hwang, H.; Jung, G. Y.; Lee, T. *Adv. Mater.* **2010**, *22*, 1228–1232.

(20) Lee, M. J.; Kim, S. I.; Lee, C. B.; Yin, H. X.; Ahn, S. E.; Kang, B. S.; Kim, K. H.; Park, J. C.; Kim, C. J.; Song, I.; Kim, S. W.; Stefanovich, G.; Lee, J. H.; Chung, S. J.; Kim, Y. H.; Park, Y. *Adv. Funct. Mater.* **2009**, *19*, 1587–1593.

(21) Shima, H.; Takano, F.; Muramatsu, H.; Akinaga, H.; Inoue, I. H.; Takagi, H. *Appl. Phys. Lett.* **2008**, *92*, 043510.

(22) Huang, J. J.; Kuo, C. W.; Chang, W. C.; Hou, T. H. *Appl. Phys. Lett.* **2010**, *96*, 262901.

(23) Smyth, D. M. In *The Defect Chemistry of Metal Oxides*; Oxford University Press: New York, 2000; Chapter 10.

(24) Jameson, J. R.; Fukuzumi, Y.; Wang, Z.; Griffin, P.; Tsunoda, K.; Meijer, G. I.; Nishi, Y. *Appl. Phys. Lett.* **2007**, *91*, 112101.

(25) Lue, H. T.; Liu, C. Y.; Tseng, T. Y. *IEEE Electron Device Lett.* **2002**, *23*, 553–555.

(26) Campera, A.; Iannaccone, G.; Crupi, F. *IEEE Trans. Electron Devices* **2007**, *54*, 83–89.

(27) Crupi, F.; Ciofi, C.; Germano, A.; Iannaccone, G.; Stathis, J. H.; Lombardo, S. *Appl. Phys. Lett.* **2002**, *80*, 4597–4599.

(28) Choi, B. J.; Jeong, D. S.; Kim, S. K.; Rohde, C.; Choi, S.; Oh, J. H.; Kim, H. J.; Hwang, C. S.; Szot, K.; Waser, R.; Reichenberg, B.; Tiedke, S. *J. Appl. Phys.* **2005**, *98*, 033715.

(29) Moulder, J. F.; Stickle, W. F.; Sobol, P. E.; Bomben, K. D. In *Handbook of X-ray Photoelectron Spectroscopy*; Chastain, J., King, R. C., Eds.; Physical Electronics Inc.: MN, 1995.

(30) Ohsaki, H.; Tachibana, Y.; Mitsui, A.; Kamiyama, T.; Hayashi, Y. *Thin Solid Films* **2001**, *392*, 169.

(31) Liu, G. M.; Jaegermann, W.; He, J. J.; Sundstrom, V.; Sun, L. C. *J. Phys. Chem. B* **2002**, *106*, 5814.

(32) Hossain, F. M.; Murch, G. E.; Sheppard, L.; Nowotny, J. *Defect and Diffusion Forum* **2006**, *251−252*, 1.

(33) Gu, D. F.; Dey, S. K.; Majhi, P. *Appl. Phys. Lett.* **2006**, *89*, 082907.

(34) Schierbaum, K. D.; Fischer, S.; Torquemada, M. C.; deSegovia, J. L.; Roman, E.; MartinGago, J. A. *Surf. Sci.* **1996**, *345*, 261–273.

(35) Beise, A. In *Concepts of Modern Physics*, 6th ed.; McGraw-Hill Companies: New York, 2003; p185.

(36) Kim, K. M.; Choi, B. J.; Shin, Y. C.; Choi, S.; Hwang, C. S. *Appl. Phys. Lett.* **2007**, *91*, 012907.

(37) Kim, K. M.; Hwang, C. S. *Appl. Phys. Lett.* **2009**, *94*, 122109.